Physics-Guided Machine Learning Approach to Characterizing Small-Scale Fractures in Geothermal Fields

Yingcai Zheng[1], Jiaxuan Li[1,2], Rongrong Lin[1], Hao Hu[1], Kai Gao[2], and Lianjie Huang[2]

[1]Department of Earth and Atmospheric Sciences, University of Houston, TX 77204-5007, USA

[2]Geophysics Group, Los Alamos National Laboratory, Los Alamos, NM 87545, USA

Yzheng12@uh.edu; ljh@lanl.gov

Keywords: Geothermal, fracture characterization, fracture detection, machine learning, small-scale fractures, DBNN

ABSTRACT

Characterizing fracture zones is crucial in geothermal exploration, drilling, and development. We aim to characterize small-scale fractures with scales less than the seismic wavelength. Recently, machine learning (ML) methods have been popular in interpreting large-scale faults by finding offsets in seismic images. However, such offsets may not be associated with small-scale fractures. By shooting a seismic beam from the Earth's surface to subsurface fracture zones, we can extract a receiver-beam interference pattern created by fracture-generated multiple-scattering waves in observed seismic data. The double-beam interference pattern is a two-dimensional image that carries information about the discrete fracture network pattern. Under the ideal situation (e.g., perfect data acquisition and homogeneous medium), the beam inference pattern and the discrete fracture pattern are Fourier transform pairs. However, in real-world cases, such a Fourier transform relation is perturbed. We need to train the machine learning algorithm to be able to handle such a physical constraint. To demonstrate the capability of the method for small-scale fracture characterization, we construct a subsurface model containing small-scale fractures based on the Soda Lake geothermal field. We perform seismic modeling to generate 3D seismic data and apply our method to the data to characterize the discrete fractures, which are almost invisible on conventional seismic migration images.

1. INTRODUCTION

Information on both faults and fractures is critical in understanding the subsurface stress field and potential fluid flow pathways for geothermal permeability assessment. Knowing the fracture geometries such as fracture orientation and spacing can greatly improve the ability to capture flow transport behavior (Kang *et al.*, 2011; Nick *et al.*, 2011; Kang *et al.*, 2016). Therefore, cost-effective methods for reliable detection of faults/fractures at a distance are important in geothermal exploration, drilling, and development. Here we distinguish faults and fractures. Faults are usually associated with fault surface slip, and their existence is generally interpreted in time and depth migrated seismic images. Recently, there are many progresses in using machine learning methods to detect large-scale faults (e.g., Wu and Fomel, 2018; Gao *et al.*, 2021a; Gao *et al.*, 2021b). On the other hand, fractures (or joints) appear in clusters (Gale *et al.*, 2007) and they are small-scale features in a layer and may not cause discontinuities in stacked seismic images compared to regions containing no fractures. Burns *et al.* (2007) showed that if the source-receiver line is perpendicular to the fracture plane, the common-mid-point stacked trace is the same as if there were no fractures.

Conventional fracture characterization was indirectly inferred based on the assumption that aligned fractures can cause seismic anisotropy (e.g., Thomsen, 1995). The symmetry types of the anisotropy can be the horizontally transverse isotropy (HTI) caused by a set of vertical fractures, the orthorhombic owing to two vertical fracture sets orthogonal to each other, the monoclinic because of two fracture sets that are at an angle not 90 degrees, and their geothermically tilted versions. Anisotropy can cause AVO/AVAZ (amplitude variation with offset and azimuth for the reflected waves (e.g., Rüger and Tsvankin, 1997; Lynn *et al.*, 1999; Perez *et al.*, 1999; Thomsen, 1999; Stewart *et al.*, 2002; 2003; Vasconcelos and Grechka, 2007; Far *et al.*, 2014) and shear-wave splitting (e.g., Crampin, 1985; Tatham *et al.*, 1992; Vetri *et al.*, 2003; Long, 2013; Verdon and Wustefeld, 2013). These anisotropy-related methods are based on the effective medium theory (EMT), which implicitly assumes that the distribution of fractures is spatially uniform and has one spatial scale (i.e., the distance between neighboring fractures) (e.g., David *et al.*, 1990). In reality, the distribution of natural fractures can be random, spatial clusters can emerge (Fang *et al.*, 2017), and the fracture system can exhibit multiple spatial scales (e.g., distance between neighboring fractures, sizes of the fracture clusters, distance between clusters, etc.). Because of multiple scattering and interference, the EMT-based methods can produce erroneous results for randomly distributed fractures (Fang *et al.*, 2017). The Scattering Index (SI) methodology (e.g., Willis *et al.*, 2006; Fang *et al.*, 2013a; Fang *et al.*, 2013b) is a data-based method and it used the differences in the stacked data along different azimuths. SI can yield information on fracture plane orientation. Diffraction imaging (e.g., Landa *et al.*, 2008; Landa *et al.*, 2011; Klokov and Fomel, 2012; Landa, 2012; Landa *et al.*, 2013; Schoepp *et al.*, 2015; Protasov *et al.*, 2016; Silvestrov *et al.*, 2016) tries to migrate fracture-diffracted signals to form a subsurface image. Because the amplitudes of the diffracted signals are much weaker compared with those of specular reflections from layer interfaces, isolation of the fracture diffraction is prerequisite. Non-specular imaging filtered in the local image matrix can be directly used to identify scattering/diffraction features in the subsurface (Zhu and Wu, 2010). However, these scattering-based imaging/migration methods can only provide focused scattering energy instead of the local fracture spacing and orientation. The image of scattering waves needs further interpretation to obtain the detailed spatial distribution of fractures and their connections via such as ant tracking (e.g., Pedersen *et al.*, 2002; Zhu and Wu, 2010; Aarre *et al.*, 2012).

In this paper, we apply a machine learning technique using a neural network architecture to augment the double-beam method developed by Zheng *et al.* (2013), which aims to characterize fractures in a layered medium using the interference pattern of multiple-scattering (in

1

horizontal directions) waves from fractures. In Zheng *et al.* (2013), they synthesize a group of point sources into a directional source beam to shoot it to the subsurface fracture targets. A fracture target can be a box containing multiple fractures. The source beam interacts with the fractures locally and produces a scattered beam propagating to surface receivers. The scattering direction of the receiver beam depends on the orientation and density of the fractures. Basically, the DB method extracts the interference pattern observed on the surface to obtain fracture parameters: fracture orientation, density, and fracture compliance (Schoenberg, 1980). Because of the use of a source beam and a receiver beam, the method is called the double-beam method (DB for short). Both beams are focusing Gaussian beams toward the fracture target. Hu and Zheng (2018) extended the original DB into a dipping layer case. Hu *et al.* (2018) also extended it to the case of multiple sets of irregularly distributed random fractures. Rather than using a Gaussian beam, Ding *et al.* (2017) used a different focusing beam, the Gaussian wave packet (Kiselev, 1983; Perel and Sidorenko, 2007) and were able to characterize fracture parameters in two layers at different depths. The original and the extended work of the DB method showed that DB can successfully and correctly characterize fractures in terms of fracture parameters: fracture orientation, fracture spacing and compliances, even for multiple coexisting fractures with random spacing and varying compliances in a non-flat dipping reservoir layer. However, the DB does not give us information of discrete fracture networks (DFN) because we interpreted the interference pattern using the three fracture parameters. The goal of this paper is to use neural network machine learning to interpret the interference pattern as discrete fracture network. We call our new method double-beam neural network (DBNN).

We organize the paper as follows. First, we briefly review the physics of the DB interference pattern. Secondly, we develop our new method, DBNN, and train it to obtain DFN information. Thirdly, we build a geological model based on the Soda Lake geothermal field and generate synthetic seismic datasets using an elastic finite-difference method (e.g., Coates and Schoenberg, 1995; Fang *et al.*, 2013b; Fang *et al.*, 2017), in which a fracture is modeled as a linear slip boundary condition (Schoenberg, 1980). Finally, we apply our DBNN to the synthetic dataset and demonstrate its capability for characterizing small-scale fractures.

2. METHODS
We first describe the physics of the DB interference (DBI) pattern, and then demonstrate how to use DBNN to interpret DBI as DFNs.

2.1 DBI Pattern
The DB method characterizes subsurface fractures by focusing a source-beam and a receiver-beam from the surface to a target zone in a fractured reservoir (Zheng *et al.*, 2013). The essence of the DB method is based on multiple scattering of a local incident plane wave upon a set of fractures. The scattering wavenumber $\mathbf{k}^r$ and the incident wavenumber $\mathbf{k}^s$ are related by the local fracture network geometry around the target location $\mathbf{r}_{frac}$ (Zheng *et al.*, 2013):

$$\mathbf{k}_T^r = \mathbf{k}_T^s + n\frac{2\rho}{a}\hat{f}, \quad n = -1 , \tag{1}$$

where $\mathbf{k}_T^r$ and $\mathbf{k}_T^s$ are the horizontal components of $\mathbf{k}^r$ and $\mathbf{k}^s$, respectively; $\hat{\varphi}$ is the unit vector perpendicular to the fracture plane and a is the fracture spacing (Figure 1a). Equation (1) is frequency dependent because the wavenumbers are proportional to the angular frequency ω. Both focusing beams have planar wavefronts at fractures so we can use plane wave scattering theory. Symbolically, the forward scattering process can be expressed as

$$D^{obs}\left(\mathbf{x}_r,\mathbf{x}_s,W\right) \sim g^s\left(\mathbf{r}_{frac},\mathbf{x}_s,W\right) \times S\left(\hat{f},a|\mathbf{r}_{frac},W\right) \times g^r\left(\mathbf{x}_r,\mathbf{r}_{frac},W\right), \tag{2}$$

where $D^{obs}\left(\mathbf{x}_r,\mathbf{x}_s,W\right)$ is the data, $g^s\left(\mathbf{r}_{frac},\mathbf{x}_s,W\right)$ and $g^r\left(\mathbf{x}_r,\mathbf{r}_{frac},W\right)$ are the source and receiver beams, respectively, and $S\left(\hat{f},a|\mathbf{r}_{frac},W\right)$ is the double-beam interference (DBI) pattern with complex values. We note that if (φ, a) is different (equation 1), the receiver beam propagates along a different direction and illuminates a different set of receivers on the surface (Figure 1a). We can exhaustively search all possible (φ, a) using all possible source and receiver beams and obtain $S\left(\hat{f},a\right)$ at the fracture target location and frequency. At the true values (φ, a), $\left|S\left(\hat{f},a\right)\right|$ produces high-amplitude "bright spots" (Figure 1b). Meanwhile, the amplitudes of the bright spots are proportional to the fracture compliance values.

DB has the following unique characteristics:
1) It provides the orientation, density, and fracture compliance for multiple sets of conjugate fractures as a function of space.
2) If there are no fractures, DB outputs 'no fracture'. This detection capability is important too.
3) DB is frequency dependent. Results from different frequencies should be the same and can cross validate each other.
4) DB can also characterize fractures in thin layers.
5) The performance of DB is not affected by layer reflections, multiples, or surface waves.
6) No geological interpretation step is needed. DB directly outputs the fracture parameters of interest.
7) The fracture compliance is often related to the fracture saturation property, gas or liquid filled. A large compliance is also found to be related to fluid flow property (Petrovitch *et al.*, 2013).
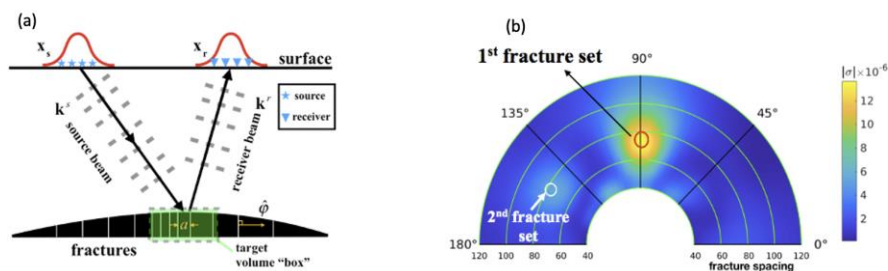
Figure 1. Schematic diagram of the DB imaging method. (a) Stars and triangles represent source and receivers, respectively. Parameter *a* is the local fracture spacing in the target area. Parameter $\hat{\varphi}$ is the fracture normal direction. (b) An example of the absolute value of the complex valued DBI pattern. Two picked bright spots indicate two detected sets of fractures. Radial direction indicates fracture spacing *a*. The polar angle is the fracture orientation *φ*. The magnitude of the bright spot indicates the fracture compliance for this set of fractures around the target.

2.2 DBNN – Interpreting DBI into DFN using neural networks

Our goal is to train a neural network to convert the complex valued DBI pattern to DFN automatically. It is an image-to-image transformation. In this section, we demonstrate this new fracture characterization using a fully connected neural network based on the DBI for each subsurface target. This new method is called DBNN. The DBNN can "learn" the nonlinear relationship between the actual fractures at one target and its synthetic DB images. We can then apply the trained DBNN to invert for the fractures within targets from the DB images obtained using surface seismic data. Under ideal acquisition conditions, DBI and DFN are Fourier transform pairs, which has a clear physical meaning; hence, DBNN is a physics-guided machine learning.
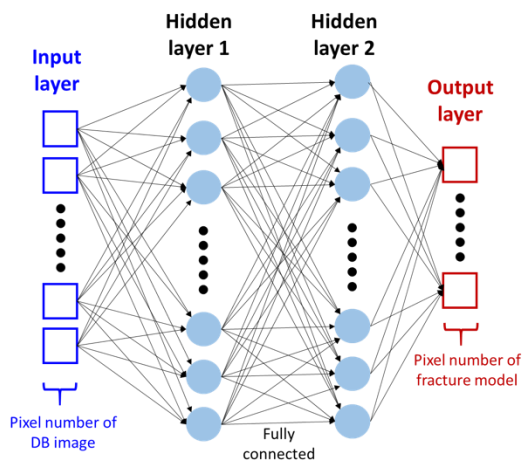

Figure 2. The architecture of our fully connected neural network for DBNN contains two hidden layers. The dropout is applied to both the input layer and hidden layers to avoid overfitting.

To automatically convert DB images to the discrete fracture distribution, we build our DBNN with four layers, including two hidden layers with each hidden layer consisting of 4000 neurons (Figure 2). A DBI (complex-value) is a 2D function of the fracture azimuth (31 angles from 0º to 180º) and the fracture spacing (30 values from 15 m to 40 m). A local 2D DFN image has 21×21 pixels covering a region of $90\ m \times 90\ m$. Both the DBI and the DFN images are flattened into 1-dimensional vectors as the input and output layer of our DBNN. Consequently, the input layer has $31 \times 30 \times 2$ (complex) neurons and the output layer has 21×21 neurons. We use dropout (Srivastava *et al.*, 2014) to both the input and hidden layers with a dropout rate of 50% to avoid overfitting in the training dataset. We use the sigmoid function as the activation function for each layer. During training, the cost function in the output layer is the mean squared differences between the DBNN predicted DFN and the true DFN. We perform our training based on the Keras (Charles, 2013) and we use the batch gradient descent and the ADAM optimizer (Kingma and Ba, 2014) with a learning rate of 0.001 to train our neural network. We train 1,000 epochs and the batch size in each epoch is 100.

In the image-to-image training process, we generate 10,000 fracture models with random fracture spacings (15 m to 40 m), orientations (0^0 to 180^0), and the number of fracture sets (1 or 2). We assume that the seismic geometry is fully covered, and data is noise-free and only contains fracture-related P waves in a homogenous layer (e.g., Zheng *et al.*, 2013; Hu and Zheng, 2018; Li *et al.*, 2019). We use this approximation to efficiently calculate the synthetic DBI using the Born modeling. One can of course use full-wave modeling (not the Born approximation) to do the training but would be more computationally expensive. We show six synthetic DFN images and their correspondent DBI in Figure 3. Then we can train our DBNN.
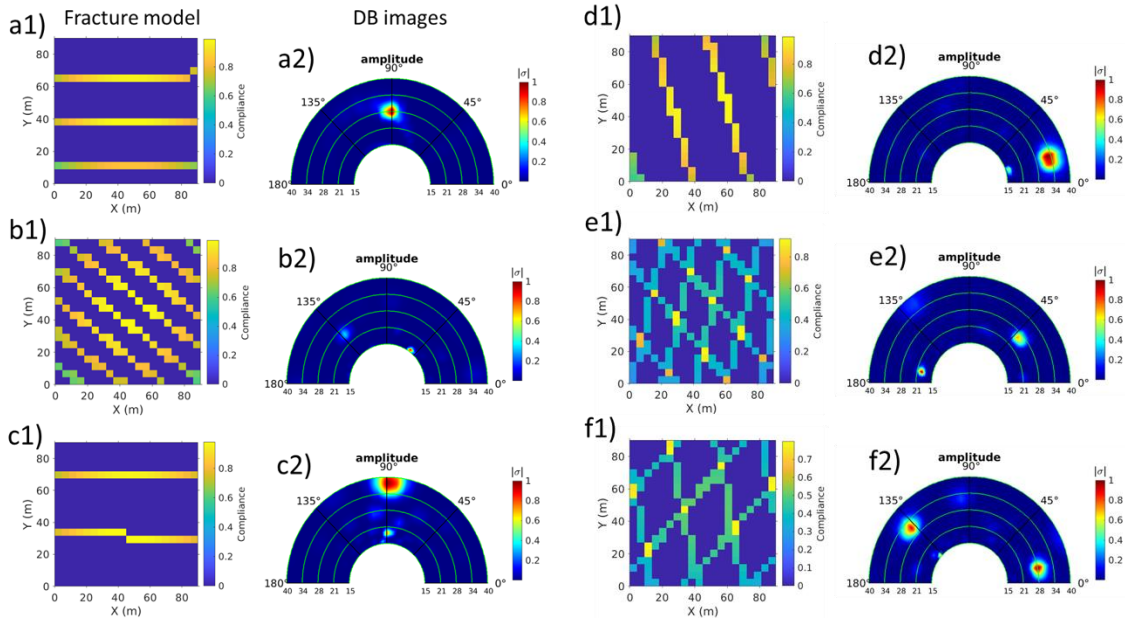
Figure 3. Examples of DFN (map view) and DBI in the DBNN training. (a1)-(f1) are six fracture models with different fracture spacing and orientation. (a2)-(f2) are their corresponding synthetic DB images. The fractures have random spacing and orientations. The spacing randomly varies from 15 m to 40m and orientation randomly varies from 0° to 180°. The number of preferred fracture sets is randomly set as 1 or 2. Panels (a) - (d) have one fracture set while (e) and (f) have two fracture sets.

Using the trained DBNN, we find that all DNFs are correctly inverted from the DBIs using our trained DBNN (Figure 4). Since DBI's are extracted from seismic data, DBNN could be used to invert for the fractures in each target using DBIs from seismic data. The inverted fractures obtained using DBNN have excellent agreement with the true fractures.
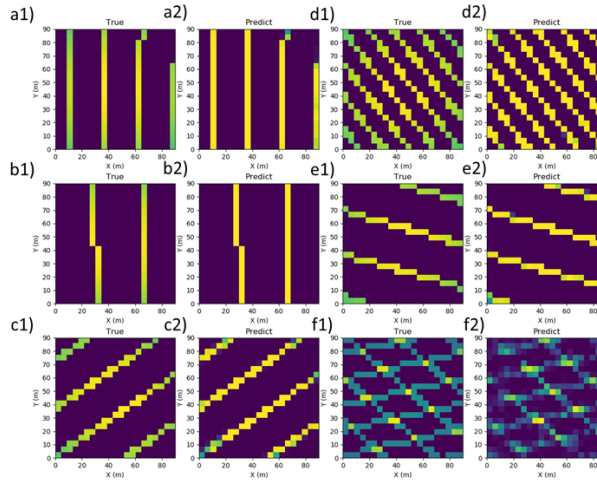

Figure 4. DBNN testing results. Panels (a1)-(f1) are six DFNs with different fracture spacings and orientations; (a2)-f(2) are the predicted DFNs using our trained DBNN from their DBIs, respectively; and (a1) to (e1) have a single fracture set while (f1) has two fracture sets. Yellow pixels represent fractures while blue pixels are background medium without fracture.

3. SYNTHETIC DATASETS AND SEISMIC MIGRATION RESULTS

We test DBNN on 3D synthetic datasets generated from a geophysical model based on the Soda Lake geothermal field (Gao *et al.*, 2021a). In this paper, we focus on DBNN application to synthetic datasets and will present field data examples in the future.

3.1 Model and dataset

We build a 3D P-wave velocity model based on the Soda Lake geothermal field (Figure 5). The S-wave velocity is half of the P-wave velocity. We use Gardner's equation (Gardner *et al.*, 1974) to convert the P-wave velocity to the density. Our forward modeling uses a 3D staggered-grid finite-difference numerical solution to the full elastic wave propagation (e.g., Fang *et al.*, 2013b; Fang *et al.*, 2017). The fractures are represented as linear slip boundaries in the finite-difference elastic forward modeling (e.g., Schoenberg, 1980; Schoenberg and Douma, 1988; Fang *et al.*, 2017; Hu *et al.*, 2018). The source wavelet is a Ricker function of 30 Hz. The grid spacing is the same in all 3 dimensions and is 4.5 m. The discretized model size is 745, 819, 133 in x, y, and z directions, respectively. The sources are regularly deployed from $x = 450\ m$ to $x = 2700\ m$ and from $y = 450\ m$ to $y = 2952\ m$, at a grid size of $18\ m \times 18\ m$. There are 17,640 distinct sources in total. The receivers are from $x = -135\ m$ to $x = 3285\ m$ and from $y = -135\ m$ to $y = 3537\ m$, at a grid size of $9\ m \times 9\ m$. For each seismic shot, we output the three-component particle velocity fields: vx, vy, vz. One example shot gather is shown in Figure 6.
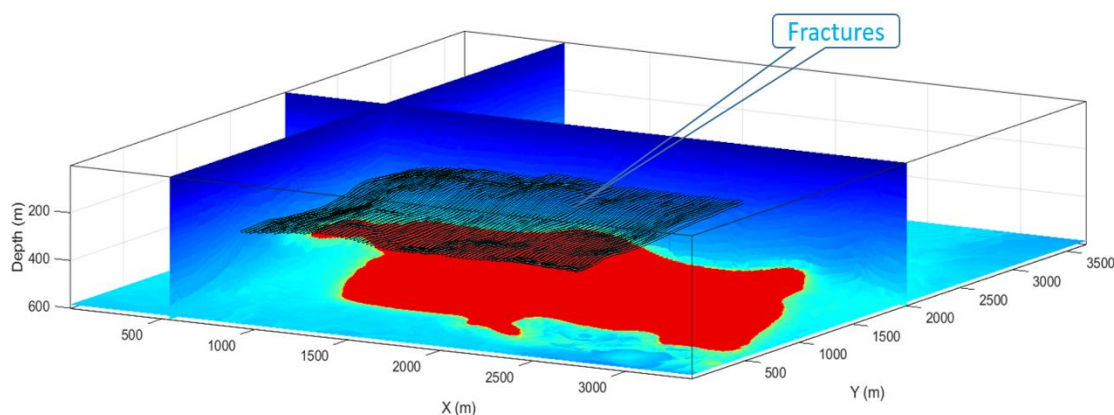

Figure 5. A 3D model showing 3D P-wave velocity, faults, and fractures. The fracture vertical height is 9m. Fractures are parallel to each other and the fracture spacing is 22.5 m. The red region is the basalt intrusion. The fracture compliance is 10^{-10} m/Pa.
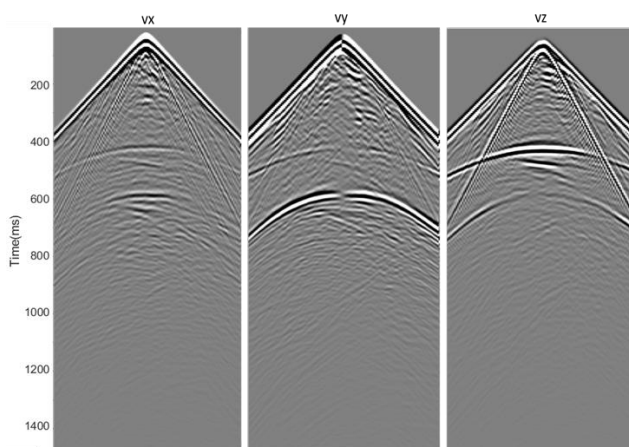

Figure 6. An example shot gather for a shot at location x=1044m, y=1008m, and the receiver line at x=1080m. The receiver line is parallel to fracture planes. The horizontal axis is the receiver line y coordinate, from 423 m to 1584 m.

3.2 Seismic migration images of fractures

One may wonder if we can see the fractures if we just do a straightforward seismic migration. We took a 2D vertical slice of the model at y=1665m. We generate two synthetic datasets with and without fractures and obtain the reverse-time migration (RTM) images (Figure 7a&b). The image difference (Figure 7c) is due to the fractures, which could be easily interpreted as a reflector horizon. In practice, we

cannot obtain such an image difference because we do not have the baseline image (Figure 7b) and all we have is Figure 7a. Identifying fractures in Figure 7a is not an easy task, if not impossible.
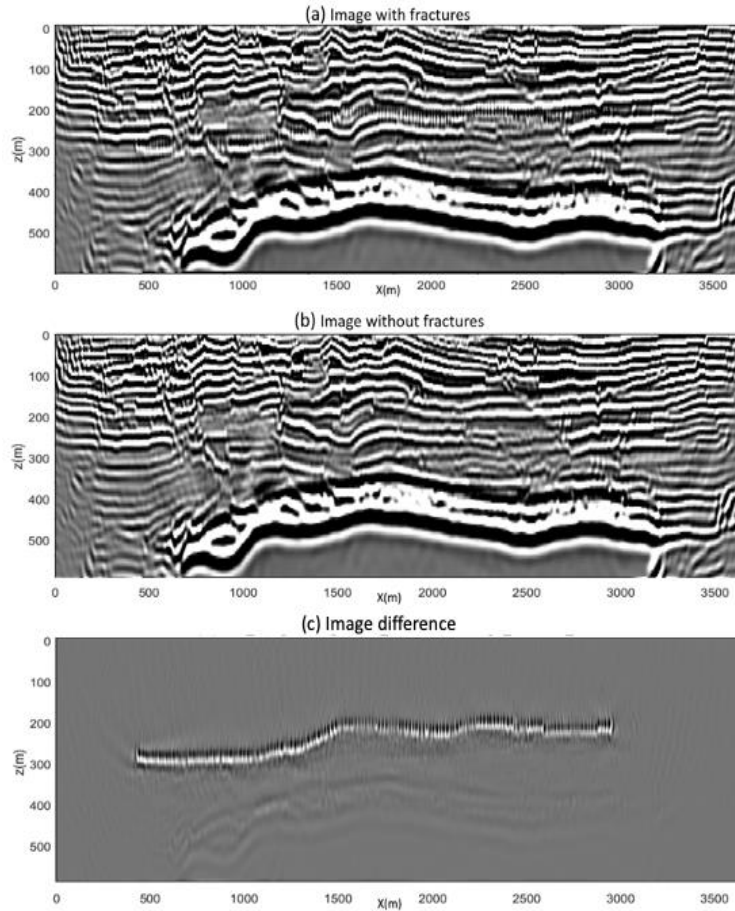

Figure 7. Seismic migration results for a set of fractures with a fracture spacing of 22.5 m and a fracture height of 9 m. (a) RTM image with fractures in the model; (b) RTM image without fractures in the model; (c) the image difference between (a) and (b).

4. DBNN RESULTS OF DISCRETE FRACTURE NETWORK CHARACTERIZATION

We apply DBNN to the 3D synthetic seismic data for the model with a fracture zone (Figure 5) to interrogate the fractures. We divide the fracture zone into 560 subsurface target bins with a bin size of $90\ m \times 90\ m$ in x and y directions. To mimic the real seismic geometry in the field acquisition and test the DBNN on limited data coverage, we randomly use only 20% of shot gathers in our DBNN test. We show DBNN results at 60 Hz for several targets in Figures 8-10.

Our DBNN is able to obtain correct results of: 1) the number of fracture sets which is one in the true model; and 2) fracture orientation that is along the y-axis. We note that DB is capable to invert for conjugate fracture sets (Figure 4f). The fractures are located at about 300 m in depth. At 60 Hz, the P-wavelength is ~40-50m. The DFN location is only less than 5 m away from the true fracture locations. Further improvement may be possible if we use multiple frequencies and more data (results in Figures 8-10 are based on only 20% of the data).

5. CONCLUSIONS

Conventional double-beam fracture characterization method extracts a double beam interference pattern from observed seismic data, and can only deliver information on fracture parameters around a target, including fracture orientation, density, and fracture compliance. Using machine learning, we have improved the capability of interpreting the complex-valued DBI as discrete fracture network (DFN). Our new method, the double beam neural network (DBNN), is an image-to-image learning method, which directly maps DBI to DFN. We have used a synthetic seismic dataset based on the Soda Lake geological model to demonstrate the capability of our DBNN for fracture characterization. DBNN can provide correct information of fracture orientation and the number of fracture sets. The location errors in the DBNN fractures are within 5 m using a 60 Hz P-wave data (wavelength ~ 40-50m) for targets at about 300 m in depth. Further improvement may be possible using multiple frequencies.
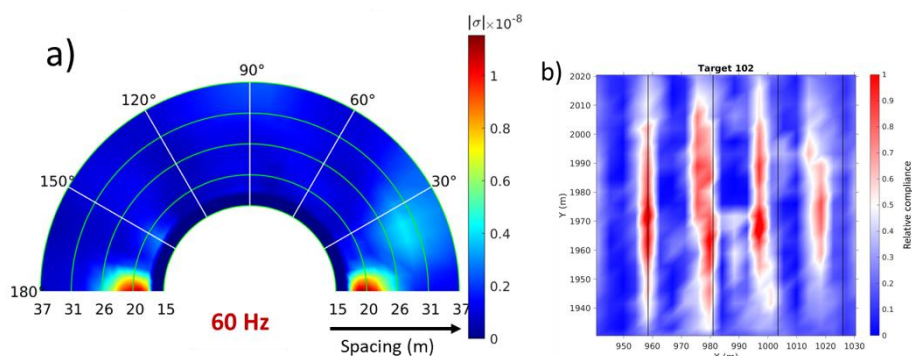
Figure 8. DBNN fracture characterization at a target (x,y) = (986 m, 1976 m). (a) The modulus of the DBI at 60 Hz using the surface seismic data. (b) Discrete fracture network (DFN) predicted by DBNN using DBI. The amplitude of the DFN indicates relative fracture compliances. The black lines along Y-axis represent the true fracture plane location in the model.
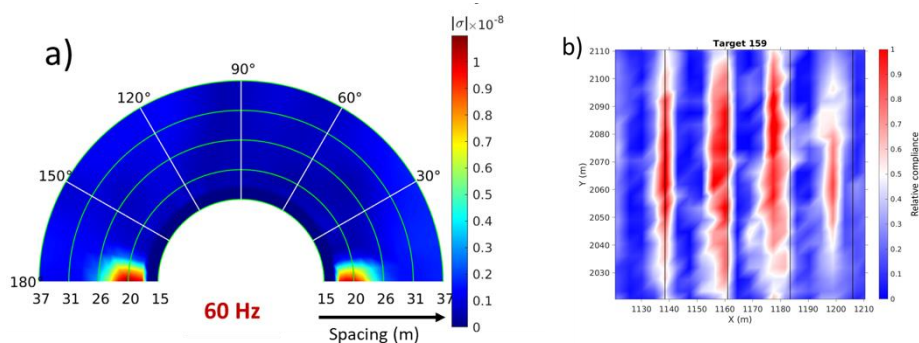

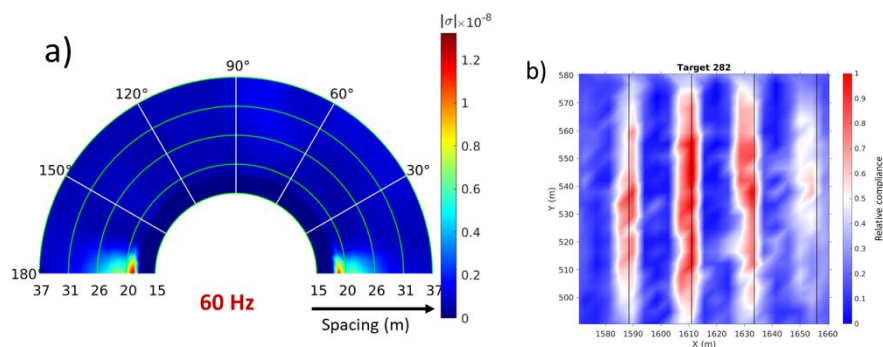**Figure 9. Same as Figure 8 but for a target (x,y) = (1166 m, 2066 m).**

Figure 10. Same as Figure 8 but for a target (x,y) = (1616 m, 536 m).

REFERENCES

Aarre, V., D. Astratti, T. N. A. Al Dayyni, S. L. Mahmoud, A. B. Clark, M. J. Stellas, J. W. Stringer, B. Toelle, O. V. Vejbæk, and G. White (2012), Seismic detection of subtle faults and fractures, *Oilfield Review*, **24**(2), 28-43.

Burns, D. R., M. E. Willis, M. N. Toksoz, and L. Vetri (2007), Fracture properties from seismic scattering, *The Leading Edge*, **26**(9), 1186-1196.

Charles, P. W. D. (2013), Project Title, *GitHub repository*.

Coates, R. T., and M. Schoenberg (1995), Finite-difference modeling of faults and fractures, *Geophysics*, *60*(5), 1514-1526.

Crampin, S. (1985), Evaluation of Anisotropy by Shear-Wave Splitting, *Geophysics*, *50*(1), 142-152.

David, C., Y. Gueguen, and G. Pampoukis (1990), Effective Medium Theory and Network Theory Applied to the Transport-Properties of Rock, *J Geophys Res-Solid*, *95*(B5), 6993-7005.

Ding, Y., Y. Zheng, H.-W. Zhou, M. Howell, H. Hu, and Y. Zhang (2017), Propagation of Gaussian wave packets in complex media and application to fracture characterization, *Geophys. J. Int.*, *210*(2), 1244-1251.

Fang, X., M. C. Fehler, Z. Zhu, Y. Zheng, and D. R. Burns (2013a), Reservoir fracture characterization from seismic scattered waves, *Geophys. J. Int.*

Fang, X., Y. Zheng, and M. Fehler (2017), Fracture clustering effect on amplitude variation with offset and azimuth analyses, *Geophysics*, *82*(1), N13-N25.

Fang, X. D., M. Fehler, T. R. Chen, D. Burns, and Z. Y. Zhu (2013b), Sensitivity analysis of fracture scattering, *Geophysics*, *78*(1), T1-T10.

Far, M. E., B. Hardage, and D. Wagner (2014), Fracture parameter inversion for Marcellus Shale, *Geophysics*, *79*(3), C55-C63.

Gale, J. F. W., R. M. Reed, and J. Holder (2007), Natural fractures in the Barnett Shale and their importance for hydraulic fracture treatments, *Aapg Bulletin*, *91*(4), 603-622.

Gao, K., L. Huang, and T. Cladouhos (2021a), Three-dimensional seismic characterization and imaging of the Soda Lake geothermal field, *Geothermics*, *90*, 101996.

Gao, K., L. Huang, R. Lin, H. Hu, Y. Zheng, and T. Cladohous (2021b), Delineating Faults at the Soda Lake Geothermal Field Using Machine Learning, *PROCEEDINGS, 46th Workshop on Geothermal Reservoir Engineering*, SGP-TR-216, Stanford University, Stanford, California

Gardner, G., L. Gardner, and A. Gregory (1974), Formation velocity and density—The diagnostic basics for stratigraphic traps, *Geophysics*, *39*(6), 770-780.

Hu, H., and Y. Zheng (2018), 3D seismic characterization of fractures in a dipping layer using the double-beam method, *Geophysics*, *83*(2), V123-V134.

Hu, H., Y. Zheng, X. Fang, and M. C. Fehler (2018), 3D seismic characterization of fractures with random spacing using the double-beam method, *Geophysics*, *83*(5), M63-M74.

Kang, P. K., M. Dentz, and R. Juanes (2011), Predictability of anomalous transport on lattice networks with quenched disorder, *Phys Rev E*, *83*(3), 030101.

Kang, P. K., Y. Zheng, X. Fang, R. Wojcik, D. McLaughlin, S. Brown, M. C. Fehler, D. R. Burns, and R. Juanes (2016), Sequential approach to joint flow-seismic inversion for improved characterization of fractured media, *Water Resources Research*, *52*(2), 903-919.

Kingma, D. P., and J. Ba (2014), Adam: A Method for Stochastic Optimization, *CoRR*, ***abs/1412.6980***.

Kiselev, A. P. (1983), Modulated Gaussian beams, *Radiophys Quant El+*, *26*(8), 755-761.

Klokov, A., and S. Fomel (2012), Separation and imaging of seismic diffractions using migrated dip-angle gathers, *Geophysics*, *77*(6), S131-S143.

Landa, E. (2012), Seismic diffraction: where's the value?, *2012 SEG Annual Meeting*,

Landa, E., S. Fomel, and M. Reshef (2008), Separation, imaging, and velocity analysis of seismic diffractions using migrated dip-angle gathers, in *SEG Technical Program Expanded Abstracts 2008*, edited,vol. pp. 2176-2180Vol. Series editor Society of Exploration Geophysicists.

Landa, E., A. Klokov, and R. Baina (2011), Point and Edge Diffractions in Three Dimensions, *73rd EAGE Conference and Exhibition incorporating SPE EUROPEC 2011*,

Landa, E., G. Reshetova, and V. Tcheverda (2013), Exploding Reflectors Revisited: 3D Heterogeneous Multiscale Elastic Media, *2013 SEG Annual Meeting*,

Li, J., H. Hu, and Y. Zheng(2019), Physics-guided machine learning identification of discrete fractures from double beam images, *SEG, Expanded abstracts*, San Antonio,

Long, M. D. (2013), Constraints on subduction geodynamics from seismic anisotropy, *Rev Geophys*, *51*(1), 76-112.

Lynn, H. B., W. E. Beckham, K. M. Simon, C. R. Bates, M. Layman, and M. Jones (1999), P-wave and S-wave azimuthal anisotropy at a naturally fractured gas reservoir, Bluebell-Altamont Field, Utah, *Geophysics*, *64*(4), 1312-1328.

Nick, H. M., A. Paluszny, M. J. Blunt, and S. K. Matthai (2011), Role of geomechanically grown fractures on dispersive transport in heterogeneous geological formations, *Physical Review E*, *84*(5), 056301.

Pedersen, S. I., T. Randen, L. Sonneland, and Ø. Steen (2002), Automatic fault extraction using artificial ants, in *SEG Technical Program Expanded Abstracts 2002*, edited,vol. pp. 512-515Vol. Series editor Society of Exploration Geophysicists.

Perel, M. V., and M. S. Sidorenko (2007), New physical wavelet 'Gaussian wave packet', *J Phys a-Math Theor*, *40*(13), 3441-3461.

Perez, M. A., R. L. Gibson, and M. N. Toksoz (1999), Detection of fracture orientation using azimuthal variation of P-wave AVO responses, *Geophysics*, *64*(4), 1253-1265.

Petrovitch, C. L., D. D. Nolte, and L. J. Pyrak-Nolte (2013), Scaling of fluid flow versus fracture stiffness, *Geophys. Res. Lett.*, *40*(10), 2076-2080.

Protasov, M. I., G. V. Reshetova, and V. A. Tcheverda (2016), Fracture detection by Gaussian beam imaging of seismic data and image spectrum analysis, *Geophys Prospect*, *64*(1), 68-82.

Rüger, A., and I. Tsvankin (1997), Using AVO for fracture detection: Analytic basis and practical solutions, *The Leading Edge*, *16*(10), 1429-1434.

Schoenberg, M. (1980), Elastic wave behavior across linear slip interfaces, *Journal of the Acoustical Society of America*, *68*(5), 1516-1521.

Schoenberg, M., and J. Douma (1988), ELASTIC WAVE-PROPAGATION IN MEDIA WITH PARALLEL FRACTURES AND ALIGNED CRACKS, *Geophysical Prospecting*, *36*(6), 571-590.

Schoepp, A., S. Labonte, and E. Landa (2015), Multifocusing 3D diffraction imaging for detection of fractured zones in mudstone reservoirs: Case history, *Interpretation-J Sub*, **3**(1), Sf31-Sf42.

Silvestrov, I., R. Baina, and E. Landa (2016), Poststack diffraction imaging using reverse-time migration, *Geophys Prospect*, **64**(1), 129-142.

Srivastava, N., G. Hinton, A. Krizhevsky, I. Sutskever, and R. Salakhutdinov (2014), Dropout: a simple way to prevent neural networks from overfitting, *J. Mach. Learn. Res.*, **15**(1), 1929-1958.

Stewart, R. R., J. E. Gaiser, R. J. Brown, and D. C. Lawton (2002), Converted-wave seismic exploration: Methods, *Geophysics*, **67**(5), 1348-1363.

Stewart, R. R., J. E. Gaiser, R. J. Brown, and D. C. Lawton (2003), Converted-wave seismic exploration: Applications, *Geophysics*, **68**(1), 40-57.

Tatham, R. H., M. D. Matthews, K. K. Sekharan, C. J. Wade, and L. M. Liro (1992), A Physical Model Study of Shear-Wave Splitting and Fracture Intensity, *Geophysics*, **57**(4), 647-652.

Thomsen, L. (1995), Elastic anisotropy due to aligned cracks in porous rock, *Geophysical Prospecting*, **43**(6), 805-829.

Thomsen, L. (1999), Converted-wave reflection seismology over inhomogeneous, anisotropic media, *Geophysics*, **64**(3), 678-690.

Vasconcelos, I., and V. Grechka (2007), Seismic characterization of multiple fracture sets at Rulison Field, Colorado, *Geophysics*, **72**(2), B19-B30.

Verdon, J. P., and A. Wustefeld (2013), Measurement of the normal/tangential fracture compliance ratio (ZN/ZT) during hydraulic fracture stimulation using S-wave splitting data, *Geophys Prospect*, **61**, 461-475.

Vetri, L., E. Loinger, J. Gaiser, A. Grandi, and H. Lynn (2003), 3D/4C Emilio: Azimuth processing and anisotropy analysis in a fractured carbonate reservoir, *The Leading Edge*, **22**(7), 675-679.

Willis, M. E., D. R. Burns, R. Rao, B. Minsley, M. N. Toksoz, and L. Vetri (2006), Spatial orientation and distribution of reservoir fractures from scattered seismic energy, *Geophysics*, **71**(5), O43-O51.

Wu, X., and S. Fomel (2018), Automatic fault interpretation with optimal surface voting, *Geophysics*, **83**(5), O67-O82.

Zheng, Y. C., X. D. Fang, M. C. Fehler, and D. R. Burns (2013), Seismic characterization of fractured reservoirs by focusing Gaussian beams, *Geophysics*, **78**(4), A23-A28.

Zhu, X., and R.-S. Wu (2010), Imaging diffraction points using the local image matrices generated in prestack migration, *Geophysics*, **75**(1), S1-S9.